Laser and Particle Beams (2017), *35*, 415–428.

doi:10.1017/S0263034617000404

Simulation of femtosecond laser absorption by metallic targets and their thermal evolution

A. SUSLOVA AND A. HASSANEIN

Center for Materials Under Extreme Environment (CMUXE), School of Nuclear Engineering, Purdue University, West Lafayette, IN 47907, USA

(RECEIVED 24 April 2017; ACCEPTED 17 May 2017)

Abstract

The interaction of femtosecond laser with initially cold solid metallic targets (Al, Au, Cu, Mo, Ni) was investigated in a wide range of laser intensity with focus on the laser energy absorption efficiency. Our developed simulation code (FEMTO-2D) is based on two-temperature model in two-dimensional configuration, where the temperature-dependent optical and thermodynamic properties of the target material were considered. The role of the collisional processes in the ultrashort pulse laser–matter interaction has been carefully analyzed throughout the process of material transition from the cold solid state into the dense plasma state during the pulse. We have compared the simulation predictions of the laser pulse absorption with temperature-dependent reflectivity and optical penetration depth to the case of constant optical parameters. By considering the effect of the temporal and spatial (radial) distribution of the laser intensity on the light absorption efficiency, we obtained a good agreement between the simulated results and available experimental data. The appropriate model for temperature-dependent optical parameters defining the laser absorption efficiency will allow more accurate simulation of the target thermal response in the applications where it is critical, such as prediction of the material damage threshold, laser ablation threshold, and the ablation profile.

Keywords: Absorption; Femtosecond laser; Thermal and optical properties; Two-temperature model; Warm dense matter

1. INTRODUCTION

In the last two decades, the interaction of ultrashort-pulsed laser (USPL) with matter has attracted great research interests, because of its numerous applications in the fields of precision micromachining (Wang *et al.*, 2013), laser-induced breakdown spectrometry (Sigman, 2010), laser ablation inductively coupled plasma mass spectrometry (Watling *et al.*, 1997; Pisonero *et al.*, 2007; Zhang *et al.*, 2013), fast chemical reactions, etc. Understanding the physical processes involved in the laser–target interaction is critical in gaining a comprehension of the entire process in all its complex nature. Sophisticated simulation models became a very popular tool of investigation that help to enhance the physics and allow minimizing the extensive experimental costs for optimization of the laser and target parameters for specific applications. In general, three major processes are considered in the theoretical analysis of the laser pulse–metal interaction, namely: absorption of the laser energy through photon–electron coupling within the thin layer during the laser pulse; heat redistribution between the electron and lattice subsystems in the picosecond time domain; and heat dissipation into the bulk of the target via electron thermal conduction (Wellershoff *et al.*, 1999; Rethfeld *et al.*, 2002; Du *et al.*, 2010). Significant research efforts have been focused on the analysis of the heat redistribution after the laser pulse, assuming constant laser absorption efficiency independent of the laser parameters. Several simulation models based on the two-temperature model (TTM) have been developed to predict the target thermal response to the femtosecond laser irradiation under varying laser and material parameters. The main assumption for TTM is a strong thermal non-equilibrium state between the electron and lattice subsystems on the picosecond time scale due to unique characteristics of the ultrashort pulse lasers (Qiu & Tien, 1993; Rethfeld *et al.*, 2002; Gamaly, 2011). Therefore, the model considers electrons and lattice as two separate thermodynamic subsystems.

The temperatures of the electron and lattice subsystems are defined from a system of the regular thermal diffusion equations for each particle type with an energy exchange term

Address correspondence and reprint requests to: A. Suslova, Center for Materials under Extreme Environment, School of Nuclear Engineering, Purdue University, West Lafayette, IN 47907, USA. E-mail: asuslova@purdue.edu

added [Eqs (1) and (2)] (Spitzer & Härm, 1953; Anisimov *et al.*, 1974). Theoretical analysis and the experimental data accumulated over decades of research demonstrate a strong temperature dependence of the thermodynamic and optical parameters included in the TTM. A variety of models were developed to account for temperature-dependent electron thermal conductivity (Chen *et al.*, 2005; Kirkwood *et al.*, 2009), electron (Chen *et al.*, 2005; Lin *et al.*, 2008; Kirkwood *et al.*, 2009), and lattice (Waldecker *et al.*, 2016) heat capacities, and electron–phonon coupling factor (Chen *et al.*, 2005; Lin *et al.*, 2008; Loboda *et al.*, 2011). However, the majority of the existing simulation models for femtosecond laser–metal interaction based on the TTM assume constant optical parameters for the target (Chen & Beraun, 2003; Chen *et al.*, 2005, 2010, 2011*a*, *b*; Zhao, 2014; Zhang *et al.*, 2015), potentially leading to inadequate estimation of the amount of energy deposited into the target during the laser pulse. This work demonstrates the effect of temperature-dependent reflectivity and optical absorption depth on the simulated laser absorption efficiency and, as a result, on the material thermal response for various metallic targets, for example, aluminum, gold, copper, molybdenum, and nickel. To adequately benchmark the simulation results and the available experimental data, we considered a two-dimensional (2D) axisymmetric model with cylindrical coordinates (r, z) assuming it was sufficient to describe the 3D behavior of the laser–material interaction.

2. MODEL DESCRIPTION AND THEORY

2.1. Two-temperature model

To accurately simulate the target thermal response to femtosecond laser irradiation, we utilized a TTM expressed as follows.

$$C_e\frac{\partial T_e}{\partial t} = \nabla k_e(\nabla T_e) - G(T_e - T_l) + S(r,z,t), \tag{1}$$

$$C_l\frac{\partial T_l}{\partial t} = \nabla k_l(\nabla T_l) + G(T_e - T_l), \tag{2}$$

where the subscript e refers to electrons and subscript l refers to the lattice, C is the heat capacity, k is the thermal conductivity, G is the coupling factor that describes the heat exchange between the electrons and the lattice, and S is the volumetric laser energy deposition rate.

For 3D simulations of the target response to laser irradiation, we have developed computer code for 2D calculations – FEMTO-2D – based on the expression of the heat conduction equations for the electron and lattice subsystems in axially symmetric cylindrical coordinates (r, z):

$$C_e\frac{\partial T_e}{\partial t} = \frac{1}{r}\frac{\partial}{\partial r}\left(k_e r\frac{\partial T_e}{\partial r}\right) + \frac{\partial}{\partial z}k_e\frac{\partial T_e}{\partial z} - G(T_e - T_l) + S(r,z,t), \tag{3}$$

$$C_l\frac{\partial T_l}{\partial t} = \frac{1}{r}\frac{\partial}{\partial r}\left(k_l r\frac{\partial T_l}{\partial r}\right) + \frac{\partial}{\partial z}k_e\frac{\partial T_e}{\partial z} + G(T_e - T_l), \tag{4}$$

where r is the radial distance from the center of the beam and z is the coordinate normal to the sample surface with the origin at the surface.

A perfect, homogeneous, and isotropic metal was assumed in the simulations. The following initial and boundary conditions were applied to solve Eqs (3) and (4). The simulation started at time $t = 0$. The initial temperature for electrons and lattice, as well as the temperatures far away from the exposed surface in the z-direction and far from the center in the r-direction at any time step are set to be at the ambient temperature (300 K).

Thermal emission from the surface of the target during simulation was accounted for with the Stefan–Boltzman law. For the other outer boundaries, zero heat losses to the surrounding vacuum were assumed during the entire calculation time: $dT_e/dr|_0 = dT_l/dr|_0 = dT_e/dr|_r = dT_l/dr|_r = 0$, and $dT_e/dz|_z = dT_l/dz|_z$.

2.2. Thermal physical parameters

At any simulation time step, the electron and lattice temperatures were numerically calculated by solving Eqs (3) and (4). To solve the equations, we needed to define the target parameters C_e, k_e, and G as functions of electron temperature, and C_l, k_l as functions of lattice temperature.

The electron heat capacity in the entire temperature diapason was defined via smooth interpolation between two polar states of the material: the cold solid state $C_e^s = (1/2)\pi^2 n_e(k_B^2 T_e/\varepsilon_F)$ and the hot plasma state $C_e^{pl} = (3/2)n_e k_B$ as following:

$$\left(\frac{1}{C_e}\right)^2 = \left(\frac{1}{C_e^s}\right)^2 + \left(\frac{1}{C_e^{pl}}\right)^2$$

giving

$$C_e = n_e k_B\frac{3\pi^2 T_e}{\sqrt{36T_F^2 + 4\pi^4 T_e^2}}, \tag{5}$$

where $n_e = Zn_i$ is electron density, Z is the average charge state at given T_e, n_i is the ion density, T_F is Fermi temperature, and k_B is Boltzmann constant.

The electron heat conductivity was also approximated by the interpolation between the cold solid state and the dense plasma state as follows:

$$k_e = \sqrt{k_e^{s2} + k_e^{pl2}} \tag{6}$$

where $k_e^s = C_e v_F^2/3\nu_{eff}$ is the heat conductivity of cold solid metal (Kittel, 2005), and k_e^{pl}=128 $(0.24 + Z)n_e T_e/3\pi(4.2 + Z)m_e(\nu_{e-i} + \nu_{e-e})$ is the plasma Spitzer heat conductivity (Kirkwood *et al.*, 2009), which was modified to

https://doi.org/10.1017/S0263034617000404 Published online by Cambridge University Press

include electron–electron collisions to consider the plasma at a near solid density.

Collision frequencies ν_{e-i}, ν_{e-e} correspond to electron–ion, electron–electron collisions in the dense plasma state, ν_{eff} corresponds to the total electron–electron and electron–phonon collision frequency in the solid metal, m_e is electron mass, and υ_F is Fermi velocity. Collision processes inside the target are discussed in greater details in the following section.

The lattice heat capacity was calculated from the Debye model of phonon's heat capacity for metals as following:

$$C_l = 9n_i k_B \left(\frac{T_l}{\theta_D}\right)^3 \int_0^{\theta_D/T_l} \frac{x^4 \exp(x)}{[\exp(x)-1]^2} dx \tag{7}$$

where $\theta_D = \hbar C_s/k_B(6\pi^2 n_i)^{1/3}$ is the Debye temperature, C_S is speed of sound in the material, $\hbar$ is the reduced Planck constant.

The lattice heat conductivity is usually omitted as negligibly small (Jiang & Tsai, 2005; Lee *et al.*, 2011) or assumed to be about 1% of the thermal conductivity of the bulk metal (Chen *et al.*, 2010, 2011*b*). In the presented model, we approximated the lattice heat conductivity based on the collision theory as follows:

$$k_l = \frac{1}{3} C_l \frac{\vartheta_i^2}{\nu_{i-i}}, \tag{8}$$

where $\vartheta_i = \sqrt{(2k_B T_l/m_i) + C_s^2}$ is the ion/phonon velocity at given lattice temperature, and $\nu_{i-i} = n_i \pi (2r_0)^2 \vartheta_i$ is the ion–ion collisional frequency calculated based on hard sphere model, m_i is atomic mass, and r_0 is atomic radius.

The rate of the heat transfer from the electron subsystem into the lattice subsystem is defined by the coupling factor. Early theoretical models usually assumed a constant value for the coupling factor (Chen & Beraun, 2003; Ibrahim *et al.*, 2003; Wang *et al.*, 2006; Liu, 2007), which is proved to be a reliable assumption at low electron temperatures. However, at the intermediate and high electron temperature range, the coupling factor is, in fact, a temperature-dependent parameter, and it has a great impact on how well the model predicts the electron and lattice temperature distributions and equilibration processes (Waldecker *et al.*, 2016). For the FEMTO-2D model, electron–phonon coupling factor on the wide electron temperature range (up to about 4.3 eV) was adopted from Lin *et al.* model (Lin, 2007; Lin *et al.*, 2008). Their model takes into account the electron density of states (DOS) in the material because the electron–phonon coupling factor is very sensitive to details of the electronic structure of the material, and thermal excitation of the electrons below the Fermi level begins to contribute to the energy transfer between electrons and phonons as laser intensity increases (Lee *et al.*, 2011). The model for the coupling factor was further extended to higher electron temperature range with the formula for electron–ion coupling in plasma: $G = 3(m_e/m_i)\nu_{e-i}\ Zn_i k_B$. At the intermediate electron temperature, above 4.3 eV, we assumed a constant value for coupling factor as long as $G_{e\text{-}ph}$ (4.3 eV) > G_{pl}.

One critical parameter included in the formulas above to calculate the thermal physical properties of the materials is an average charge state. Different approaches and simulation models for the electron DOS and the average charge state calculation currently exist and are utilized by the research community. Figure 1 shows the average charge states dependence on the electron temperature for the materials of interest used in our model for the wide temperature diapason from room temperature up to 100 eV. At electron temperatures above 4 eV, we used the FLYCHK code (Chung *et al.*, 2005) to calculate the average charge state for aluminum, gold, copper, molybdenum, and nickel. At lower electron temperatures (up to 2–3 eV), the FLYCHK code for dense matter is known to produce overestimated values for the average charge state (Chung *et al.*, 2005); therefore, in this temperature range, we utilized the data adopted from (Lin, 2007; Lin *et al.*, 2008) calculated based on VASP code. Smooth interpolation between the data for average charge state from VASP code and from FLYCHK code was performed were needed (e.g., for molybdenum).

2.3. Optical model for the laser energy absorption

The laser energy absorbed by the target during the pulse is described as the volumetric heat source $S(r, z, t)$ in the Eq. (1). The heat source was modeled with the Gaussian temporal and spatial (radial) profiles, and an exponential attenuation of the laser intensity with depth according to the Beer–Lambert law (Qiu & Tien, 1994):

$$S(x, r, t) = \sqrt{\frac{\beta}{\pi}} \frac{(1-R)}{t_p l_p} I_0 \exp\left[-\left(\frac{z}{l_p}\right)\right] \times \exp\left[-\frac{r^2}{2\sigma^2}\right] \exp\left[-\beta^* \left(\frac{t-2t_p}{t_p}\right)^2\right], \tag{9}$$

where I_0 is the laser peak power density, R is the temperature-dependent reflectivity, l_p is the temperature-dependent optical penetration depth, t_p is the laser pulse full width at half-maximum, and $\beta = 4\ln 2$.

The efficiency of the laser absorption is defined by the material optical properties and laser parameters. The commonly used assumption of the constant reflectivity and optical penetration depth (Chen *et al.*, 2010, 2011*b*) allows significant simplification of the calculations and saving of the computer time; however, it leads to an inaccurate estimation of the amount of heat deposited into the target and overall target response.

In the presented work, we have considered temperature-dependent reflectivity and optical penetration depth in Eq. (7) at any time step and across the spatial beam profile. These important parameters are physically dependent on the collisional processes inside the target, namely electron–phonon or electron–ion collisions, and electron–electron

https://doi.org/10.1017/S0263034617000404 Published online by Cambridge University Press

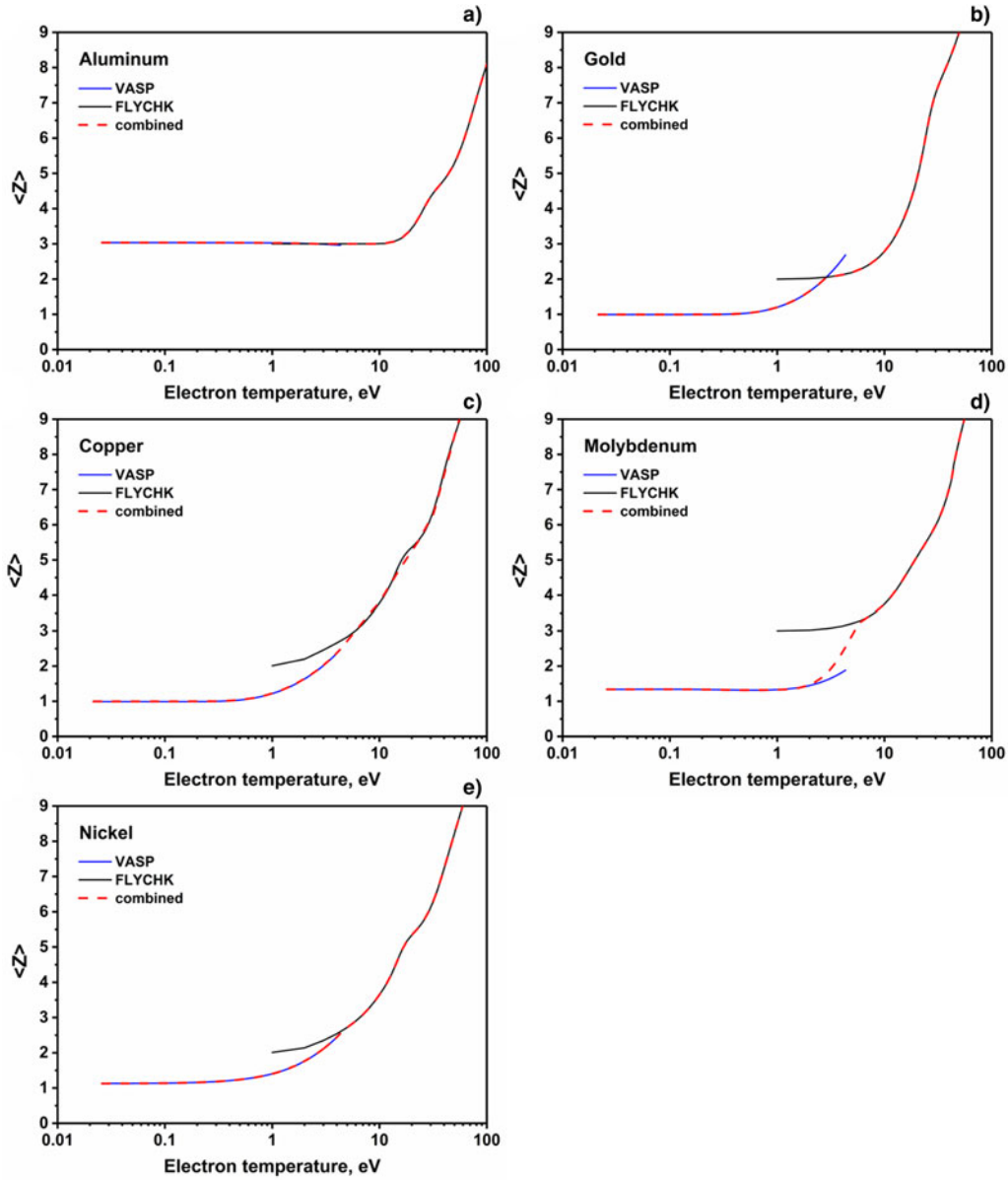

Fig. 1. Average charge state versus electron temperature for (a) aluminum, (b) gold, (c) copper, (d) molybdenum, and (e) nickel.

collisions. The surface reflectivity and optical penetration depth are related to effective electron collision rate according to the Drude absorption model via material dielectric function [Eq. (10)] by the Fresnel formula [Eq. (11)].

$$\epsilon_r = 1 - \frac{\omega_p^2}{i\omega\nu_{\text{eff}} + \omega^2}, \tag{10}$$

where $n_e = Zn_i$ is electron density, Z is the average charge state at given T_e, n_i is the ion density; $\omega_p = \sqrt{n_e e^2/\epsilon_0 m_e}$ – material plasma frequency; ω – frequency of the laser field; ν_{eff} – effective collision frequency – sum of electron–electron and electron–lattice (phonon or ion) collision frequencies. The detailed mechanism for effective collision frequency calculation is provided in the following section.

$$R = \left|\frac{1 - \sqrt{\epsilon_r}}{1 + \sqrt{\epsilon_r}}\right|^2, \tag{11}$$

where $\epsilon_r = \epsilon_1 + i\epsilon_2$ is material dielectric function – combination of material permittivity and conductivity.

Optical penetration depth was defined as the depth at which the intensity of the transmitted electromagnetic wave drops to $1/e$ of its initial value at interface (Brown & Arnold, 2010) and calculated as follows:

$$l_p = \frac{\lambda}{4\pi\, Im[\sqrt{\epsilon_r}]}, \tag{12}$$

where λ is the laser wavelength.

https://doi.org/10.1017/S0263034617000404 Published online by Cambridge University Press

Table 1. *Material properties*

	Al	Au	Cu	Mo	Ni	Ref.
Mass of ion (m_i, a.m.u)	26.98	196.97	63.55	95.96	58.69	a
Ion density (n_i, m^{-3})	6.00×10^{28}	5.90×10^{28}	8.49×10^{28}	6.41×10^{28}	9.13×10^{28}	b
Atomic radius (r_0, m)	1.84×10^{-10}	2.14×10^{-10}	1.96×10^{-10}	2.17×10^{-10}	1.97×10^{-10}	b
Debye temp. (θ_D, K)	428	165	343	450	450	a
Melting temp. (T_m, K)	933	1337	1358	2896	1728	a
Fermi temp. (T_F, K)	13.58×10^{4}	6.42×10^{4}	8.12×10^{4}	8.24×10^{4}	9.28×10^{4}	c
Speed of sound (C_S, ms^{-1})	5.10×10^{3}	3.24×10^{3}	3.57×10^{3}	6.19×10^{3}	4.97×10^{3}	a, d
Reflectivity at 800 nm, R	0.868	0.968	0.967	0.557	0.689	e
Optical depth l_p, nm	13.0	13.7	12.2	19.0	13.5	e, f, g
C_l, (J/m^3 K)	2.4	2.5	3.5	2.8	3.9	h, i

(a) – Kittel (2005), (b) – Lide (2003), (c) – Ashcroft and Mermin (1976), (d) – Samsonov (1968), (e) – Rakic *et al.* (1998), (f) – Chen *et al.* (2010), (g) – Hermann *et al.* (2006), (h) – Chen *et al.* (2011*a*), (i) – Chase (1998).

The physical, thermal, and optical parameters for five metals used in the simulations are listed in Table 1.

2.4. Collision theory

The rate of collisional processes inside the target affects most of the parameters defining the laser energy absorption and heat redistribution, including the surface reflectivity, optical penetration depth, the rate of the heat transfer from the electron subsystem into the lattice subsystem (the electron–phonon coupling factor), the rate of the heat transport into the bulk (electron and lattice thermal conduction). In the case of the femtosecond laser interaction with metal, in contrast to the longer laser pulses (e.g., picosecond scale and longer), the laser energy deposited into the target at the extremely high rate, leading to the rapid rise of the electron temperature, which results in transition of the metal from the cold solid state into the dense plasma state during the laser pulse of intermediate and high intensity. Therefore, it is necessary to consider all different states/phases the material is going through.

In the cold solid state, the dominant collision mechanism is the scattering of electrons by phonons. For these types of collisions, the collision frequency varies with the lattice temperature as follows:

$$\nu_{e-ph} = \nu^0_{e-ph}\left(\frac{T_l}{300\,\mathrm{K}}\right), \tag{13}$$

where ν^0_{e-ph} is the electron–phonon collision frequency at room temperature, and T_l is the lattice temperature.

The values for the electron–phonon collision frequency at room temperature were obtained by fitting the Drude model of the permittivity to the experimental values of permittivity, and are given in Table 2.

For the dense plasma state with the electron temperature around and above Fermi temperature, we have modified Spitzer's formula (Spitzer & Härm, 1953; Callen, 2006) for the electron–ion collision frequency in hot plasma in order to account for the electron degeneracy effect in the plasma at a solid density by including participation factor f_p as follows:

$$\nu_{e-i} = \left(\frac{4}{3\sqrt{\pi}}\right)\frac{Z^2e^4n_i}{4\pi\varepsilon_0^2}\frac{f_p}{m_e^{1/2}(2k_BT_e+2\mu)^{3/2}}\ln(\Lambda) \tag{14}$$

where ϵ_0 is the permittivity of free space, e is the charge of the electron, $\ln(\Lambda)$ is the Coulomb logarithm, μ is chemical potential, f_p is the electron participation factor.

To define the electron–lattice collision frequency in the wide temperature range from the cold solid through the warm metal state into the dense plasma states, we applied the following interpolation:

$$\nu_{e-ph/e-i} = \frac{\nu^s_{e-ph}\,\nu^{pl}_{e-i}}{\sqrt{{\nu^s_{e-ph}}^2+{\nu^{pl}_{e-i}}^2}}. \tag{15}$$

We also considered the fact that the maximum possible value for the electron–lattice collision frequency cannot exceed the theoretical value calculated based on the hard sphere model $\nu_{hs} = \sqrt{V^2_{Fermi}+(2k_BT_e/m_e)}/r_0$, where r_0 is atomic radius and V_{Fermi} is electron velocity near Fermi energy.

For the cold solid state as well as for the hot plasma state, the electron–phonon or electron–ion (respectively) collision processes are dominant over electron–electron collisions in the case of the thermal equilibrium. However, due to the strong non-equilibrium between electron and lattice subsystems and extremely dense plasma state at high electron temperature, electron–electron collisions must be taken into account when calculating effective collision frequency (Komashko, 2003; Shternin & Yakovlev, 2006): $\nu_{eff} = \nu_{e\text{-}ph/e-i} + \nu_{e-e}$, where ν_{e-e} is calculated with Eq. (16).

The electron–electron collision frequency was calculated in a similar way the electron–ion collision frequency in the dense plasma state:

$$\nu_{e-e} = \left(\frac{4}{3\sqrt{\pi}}\right)\frac{Ze^4n_i}{4\pi\varepsilon_0^2}\frac{f_p^2}{m_e^{1/2}(2k_BT_e+2\mu)^{3/2}}\ln(\Lambda). \tag{16}$$

https://doi.org/10.1017/S0263034617000404 Published online by Cambridge University Press

Table 2. *Electron–phonon collision frequency at room temperature*

	Al (a)	Au (a)	Cu (b)	Mo (c)	Ni (d)
Permittivity	−61.084 + 44.788i	−22.104 + 1.775i	−24.987 + 2.05i	1.9059 + 24.477i	−13.677 + 22.057i
ϑ^0_{e-ph}, s^{-1}	1.85×10^{15}	2.6×10^{14}	1.86×10^{14}	3.5×10^{15}	3.85×10^{15}

(a) – Rakic *et al*. (1998), (b) – Polek (2015), (c) – Ordal *et al*. (1988), (d) – Ordal *et al*. (1987).

Electron participation factor f_p is introduced to account for the electron degeneracy effect, and was estimated as following: $f_p = \frac{1}{Zn_i}\int_\mu^\infty f(\varepsilon)D(\varepsilon)d\varepsilon$, where $D(\varepsilon)$ is the electron DOS, and $f(\varepsilon)$ is the Fermi distribution at given electron temperature T_e.

Chemical potentials for listed metals on the entire electron temperature diapason were calculated from the conservation of the total number of electrons, by setting the result of the integration of the product of DOS and the Fermi distribution function at given electron temperature over all energy levels to be equal to the total number of electrons:

$$\frac{\sqrt{2m_e^3}}{\pi^2\hbar^3}\int_0^\infty \frac{\varepsilon^{1/2}}{\exp\left[\varepsilon-\mu(T_e)/k_BT_e\right]+1}d\varepsilon = Zn_i.$$

3. SIMULATION RESULTS AND DISCUSSION

3.1. Collisional processes

In the previous section, we discussed the role of the collision processes inside the target exposed to femtosecond laser irradiation as a critical parameter defining material's optical and thermal physical properties. Next, we have simulated the collisional processes for different interacting particles (electron–electron, electron–phonon, or electron–ion) inside the target exposed to such ultrashort laser. Since the primary goal for this work was to investigate the laser absorption efficiency, we limit our discussion to the time frame of the pulse duration.

Figure 2 shows how the collision rate for electron–electron and electron–lattice collisions changes in different metals during interaction with 800 nm 150 fs laser pulse of high fluence (~80 J/cm^2). At this laser intensity, the maximum electron temperature reaches tens eV (above Fermi temperature), meaning that the material changes from the cold solid state into the extremely dense plasma state during the laser pulse. As seen in Figure 2, the contribution of the electron–electron collisions to the effective collision frequency becomes considerable at the intermediate temperature range for aluminum, nickel, molybdenum, and even significantly dominates over electron–ion collisions in copper and gold.

The electron temperature rapidly increases during the laser pulse, but the changes in the lattice temperature are commonly described as not significant. However, our simulations predict a notable increase of the lattice temperature at high laser intensities. Therefore, both electron and lattice temperatures affect the effective collision frequency in the target during the laser pulse, resulting in the changes of the absorption efficiency and the laser optical penetration depth due to changes in the dielectric function in the accordance with Eqs (11) and (12).

3.2. Absorption processes

Series of simulations for different laser intensities (5×10^{11}, 5×10^{12}, 5×10^{13}, 5×10^{14}, and 1×10^{15} W/cm^2) were conducted to investigate the thermal dependence of the laser absorption efficiency. Figure 3 shows the simulation predictions and compares the absorptivity temporal profile during the laser pulse to the constant absorptivity (dashed line). At the laser intensity above 5×10^{11} W/cm^2 (corresponding to the laser fluence of ~80 mJ/cm^2), the absorptivity changes significantly following changes in the effective collision frequency. Therefore, even at low laser fluences, it is important to consider thermal dependence of the optical properties for femtosecond laser–metal interaction. Moreover, the absorptivity temporal profiles are notably different for different laser intensities; that will limit any semiempirical approach to the laser absorption efficiency estimation to specific laser parameters.

At high laser fluences (>5×10^{13} W/cm^2), electron temperature increases so rapidly that material transforms into the hot dense plasma state at the beginning of the laser pulse, and the reflectivity increases comparing to the preceding warm metal state. Another observation from the simulation results is that the reflectivity of nickel is increasing slowly with the electron temperature at the beginning of the laser pulse, but then rapidly decreases following the trend similar to other metals. The reason for such trend is unclear and could be related to how rapidly the material plasma frequency changes compared with the effective collision frequency.

Since the real laser beam has physical dimensions and a power density redistribution in space, 1D simulation model for laser absorption will be not sufficient for some applications, for instance, to simulate a heat-effected zone, material ablation, and crater profile. Figure 4 shows how the absorptivity changes across the laser beam at the

https://doi.org/10.1017/S0263034617000404 Published online by Cambridge University Press

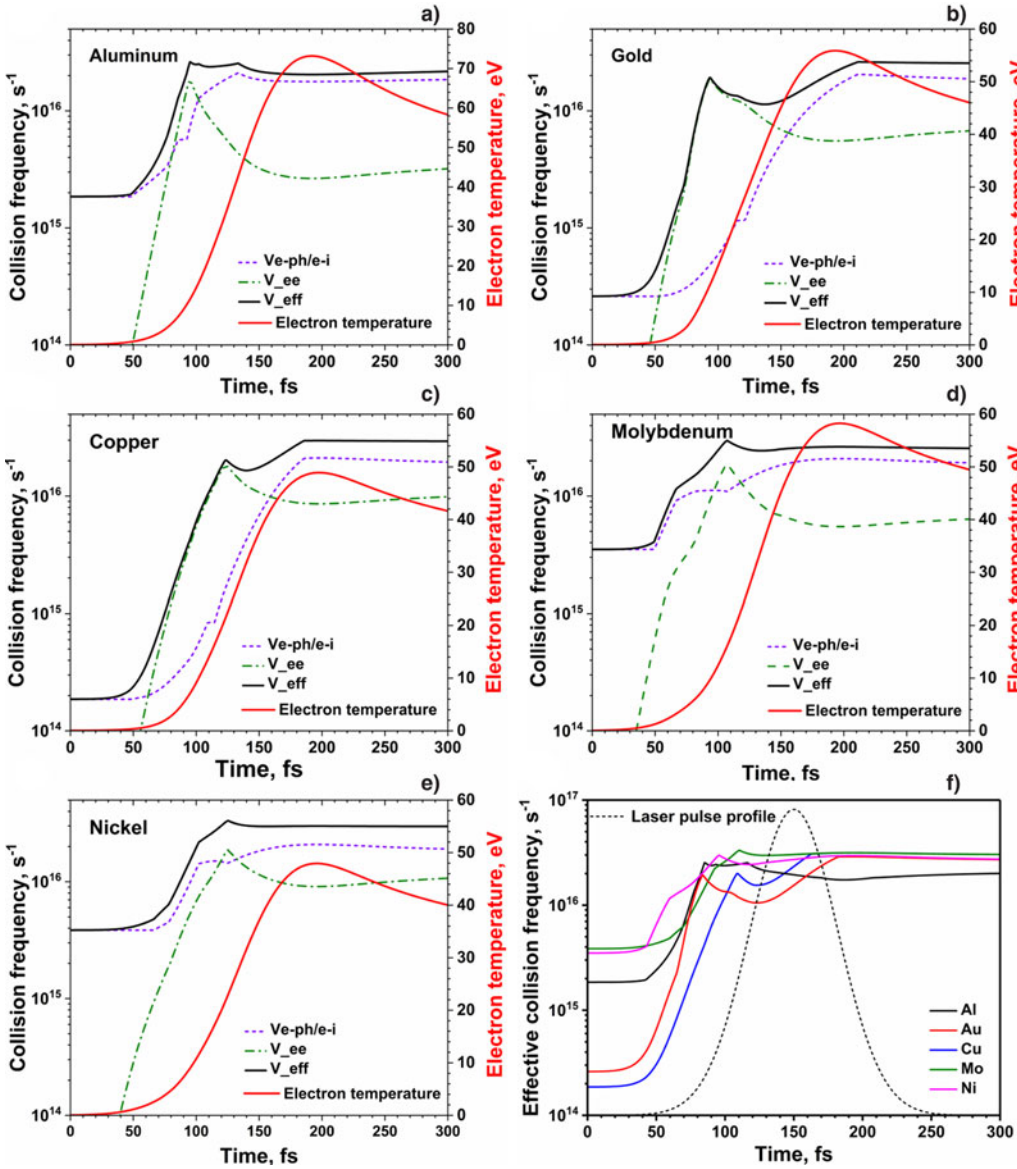

Fig. 2. Collision frequencies in (a) aluminum, (b) gold, (c) copper, (d) molybdenum, and (e) nickel targets during 150 fs laser pulse; (f) comparison of the effective collision frequencies in different metals in response to the same laser conditions. Laser parameters: λ – 800 nm, pulse duration – 150 fs, peak power density – 5×10^{14} W/cm^2.

fixed time step (150 fs) for the intermediate laser intensity of 5×10^{13} W/cm^2.

To analyze how the effective absorptivity of the metal target changes with laser intensity, the temporal and spatial distributions of absorptivity must be considered. Figure 5a demonstrates how the simulated temperature-dependent absorption varies with the laser intensity, and Figure 5b compares it to the constant absorptivity for aluminum, gold, copper, molybdenum, and nickel on the same laser intensity range.

The largest increase in the absorption efficiency normalized to the fixed value was observed for copper (about 13 times increase) and gold (around 11 times increase). Absorption for aluminum increases about 4.5 times compared with the constant value. The absorption for nickel and molybdenum does not change significantly. This can be related to how much the effective collision frequency for each metal changes with the electron temperature (Fig. 2), and may possibly be explained by the role of the electron–electron collisions as follows. Two metals, gold and copper, have similar structure of electron DOS distribution with the region of high electron DOS associated with *d*-bands that get thermally excited at the electron temperature above 1 eV (Lin *et al.*, 2008). These thermally excited electrons may significantly increase the electron–electron collision rate as observed in Fig. 2. The electron DOS distribution for aluminum, in general, follows the trend predicted with the free electron gas model (Lin *et al.*, 2008). Therefore, although the thermally

https://doi.org/10.1017/S0263034617000404 Published online by Cambridge University Press

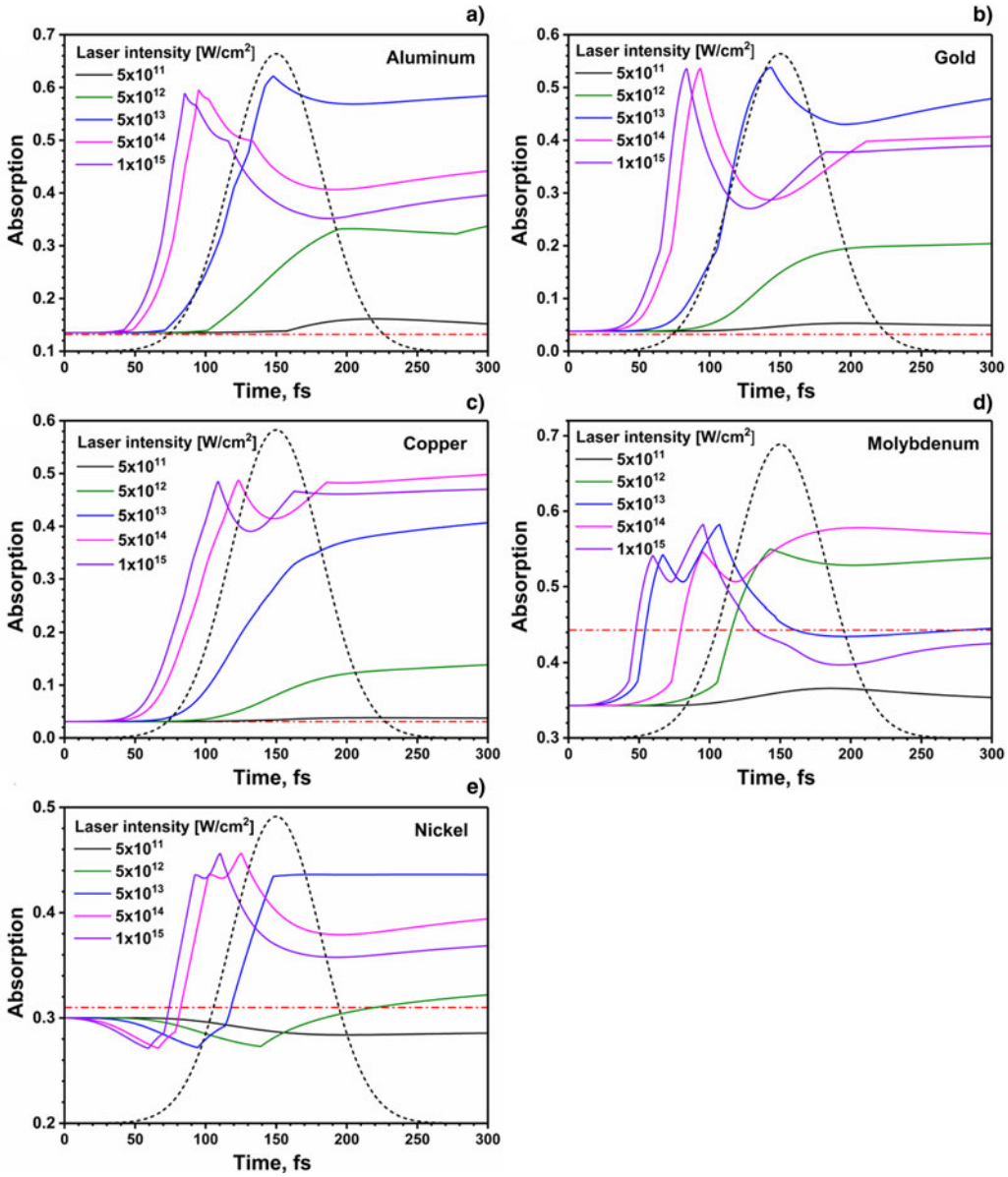

Fig. 3. Absorption in the center of the laser beam during 150 fs pulse at different laser intensities for (a) aluminum, (b) gold, (c) copper, (d) molybdenum, and (e) nickel. The red dash-dotted line corresponds to $A = 1 - R$, where R is tabulated reflectivity. The black dotted line shows laser pulse temporal profile.

excited electrons in aluminum contribute to the electron–electron collision rate, the number of these electrons is significantly lower than for copper and gold. Molybdenum and nickel belong to the group of transition metals with a complex structure of electron DOS distribution. Molybdenum has a half-filled *d*-band with small values of DOS at the Fermi level, while nickel has an almost full *d*-band with the Fermi level cutting through the high-energy edge of the band. Consequently, molybdenum has a high DOS right above the Fermi level available to the thermally excited electrons within *d*-band, and nickel has low DOS in *s*-band available for thermally excited electrons from *d*-band. Therefore, the contribution of the thermally excited electrons to the effective collision frequency is significantly reduced in molybdenum and nickel.

In general, the trend observed for absorption in all five metals at the high laser intensity of 1×10^{15} W/cm^2 is in a good agreement with the data reported by Price *et al.* (1995): at the laser intensities around 2×10^{15} W/cm^2, the absorption for aluminum, gold, copper, tantalum, and quartz has similar values of around 0.3–0.37, and temperature dependence is consistent with a "universal plasma mirror" reflectivity.

The effect of the thermally dependent absorption efficiency on the material thermal response is demonstrated in Figure 6.

https://doi.org/10.1017/S0263034617000404 Published online by Cambridge University Press

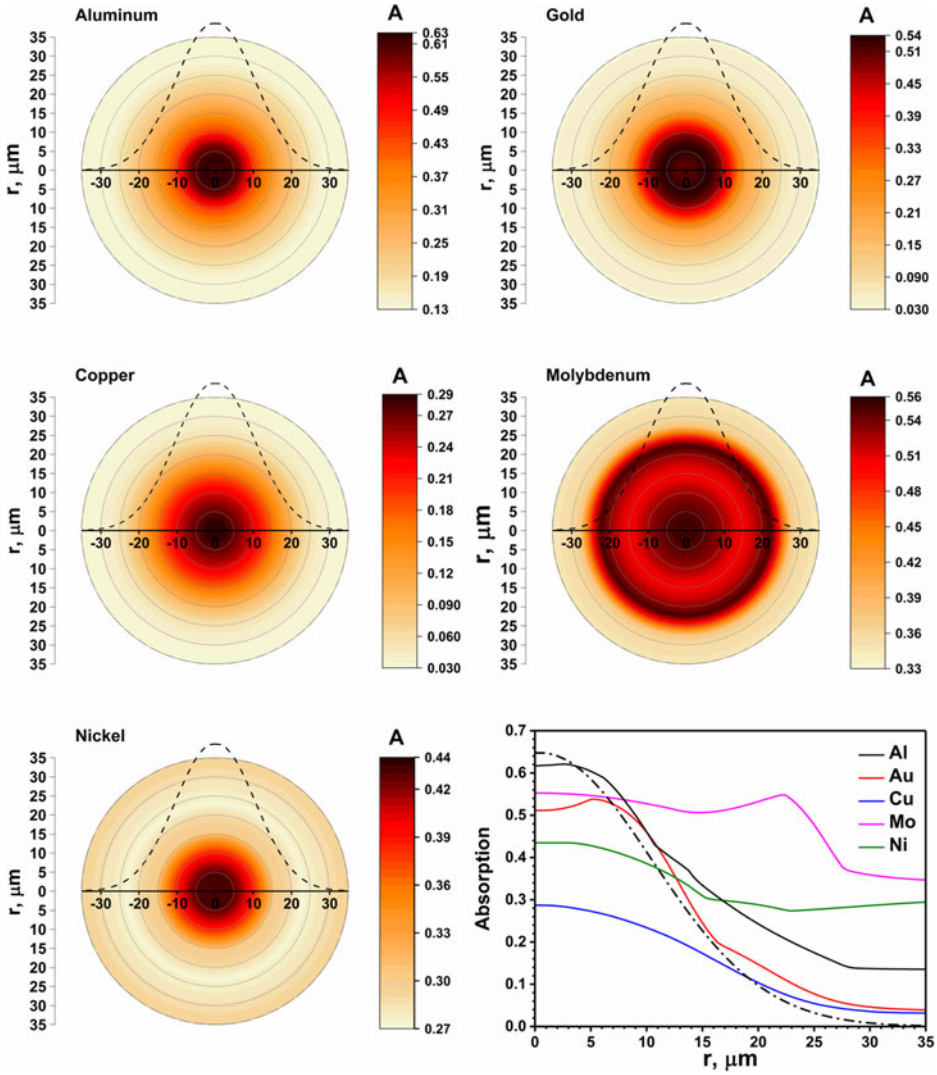

Fig. 4. Absorption across the beam profile at 150 fs simulation time step for aluminum, gold, copper, molybdenum, and nickel exposed to a laser pulse of 5×10^{13} W/cm^2. Dashed line shows laser beam spatial profile.

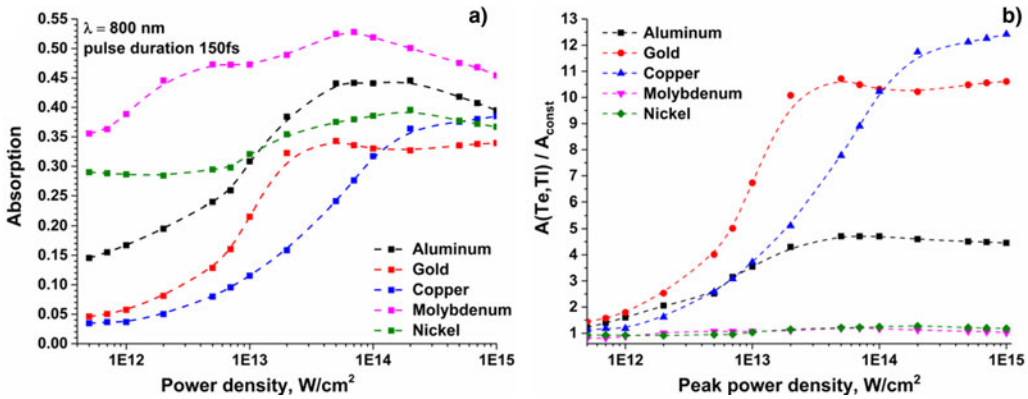

Fig. 5. Absorption versus laser intensity: (a) absolute values, (b) as ratio of constant value typically used in TTMs. Pulse duration 150 fs, wavelength 800 nm. Lines guide the eye.

https://doi.org/10.1017/S0263034617000404 Published online by Cambridge University Press

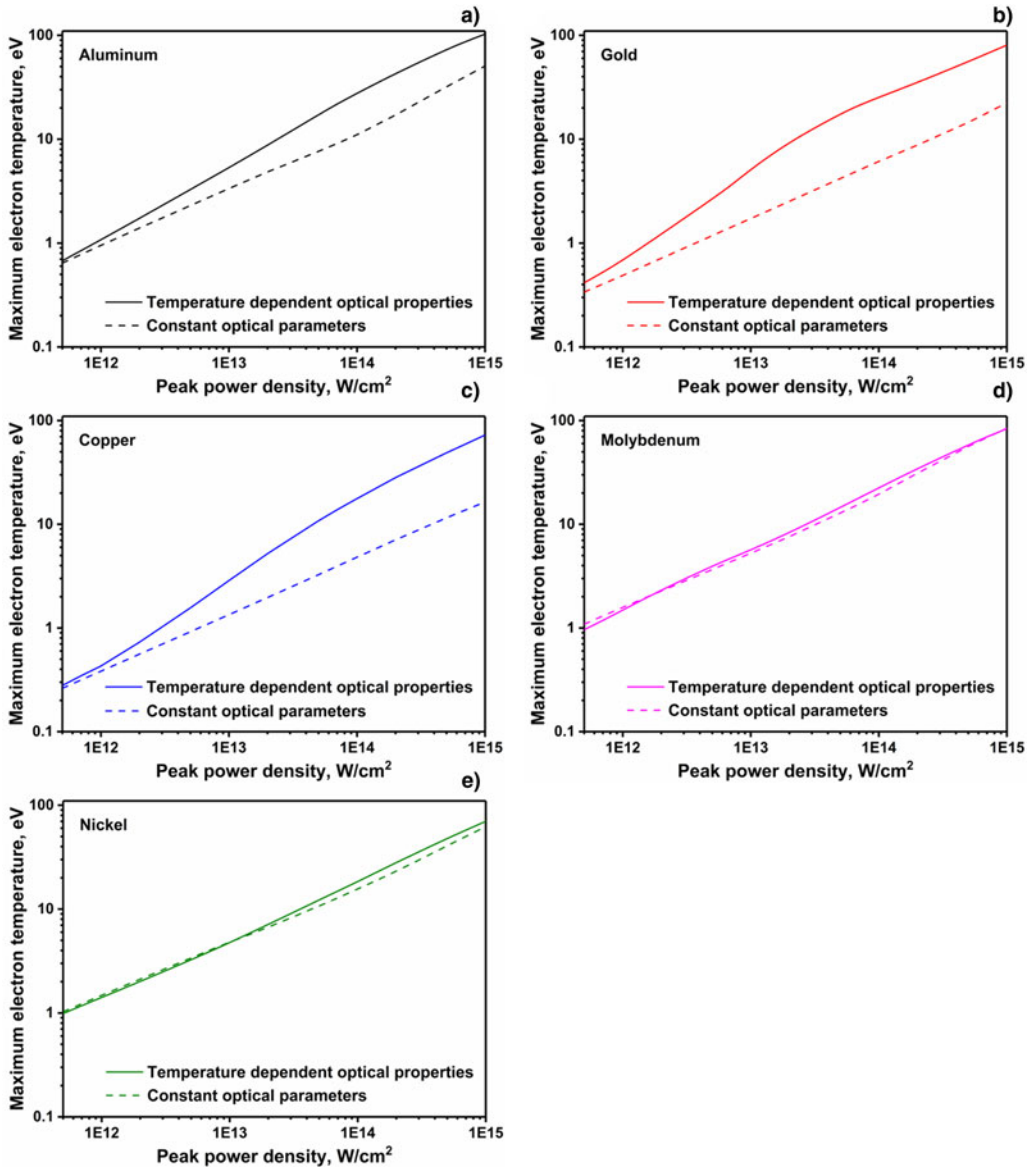

Fig. 6. Comparison of the target thermal response (maximum electron temperature) versus laser pulse intensity for two series of simulations: (1) with temperature-dependent absorption (solid line) and (2) constant value for absorption (dashed line).

As expected, the simulation predicted insignificant difference in the maximum electron temperature for molybdenum and nickel due to small changes in the absorption efficiency; however, the maximum electron temperature was greatly underestimated for aluminum, gold, and copper in the case of the constant absorption efficiency as the laser intensity increases.

3.3. Optical penetration depth

Another optical parameter, which thermal dependence is also defined by collisional processes inside the target, is the optical penetration depth. Figure 7 shows how the optical penetration depth normalized to the constant values listed in Table 1 changes with the laser intensity in the metal targets.

In general, the optical penetration depth does not directly impact how much energy is absorbed by the target; but it defines how the absorbed energy is distributed inside the target during the pulse, affecting the maximum electron temperature at the surface. Although considering thermally dependent optical penetration depth versus constant parameter may not have a significant impact on the simulation predictions of the material thermal response to the femtosecond laser irradiation, it contributes to the goal of gaining the clear understanding of the physical processes involved.

3.4. Benchmarking against available experimental data

Finally, we wanted to benchmark the theoretical predictions of FEMTO-2D model against the available experimental

https://doi.org/10.1017/S0263034617000404 Published online by Cambridge University Press

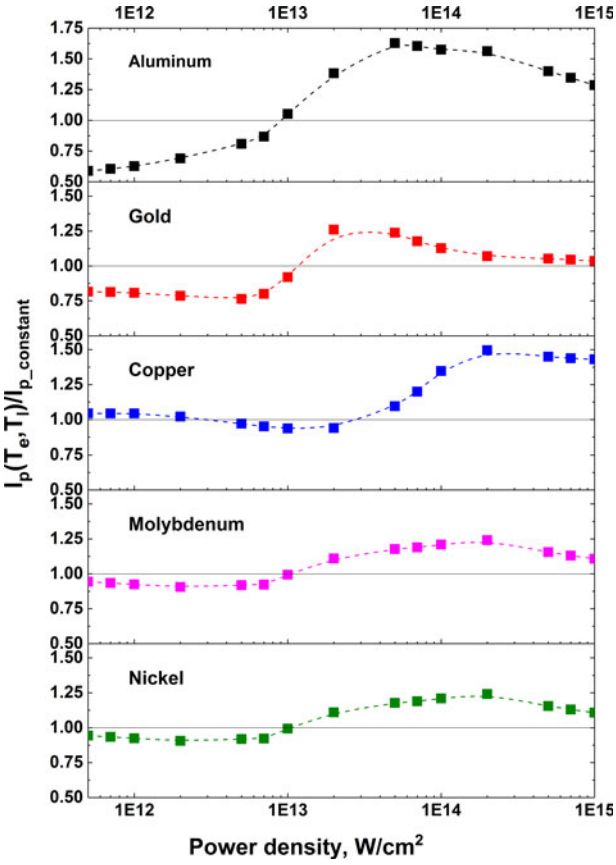

Fig. 7. Normalized optical depth versus laser intensity. Pulse duration 150 fs, wavelength 800 nm. Lines guide the eye.

data. Due to the lack of the published experimental results for femtosecond laser–metal interaction in the field of the laser absorption, we only compared the data for aluminum, gold, and copper.

For aluminum, we have benchmarked our modeling predictions against the available experimental results, as well as against simulated data from HYADES code published by Komashko (2003). Figure 8 presents the results for 400 nm wavelength with the pulse duration (a) 50 and (b) 150 fs.

As it can be seen, the numerically simulated and experimental curves exhibit similar behavior for a wide range of the laser intensities. The theoretical predictions are in a good agreement with the experimental data and HYADES code (Komashko, 2003) predictions for 50 fs laser pulses and demonstrate a good correlation with experiment for 150 fs laser pulses up to 5×10^{14} W/cm^2. However, as the intensity is further increasing, the simulation model tends to slightly overestimate the absorption compared with the experimental data. In Fisher *et al.* (2001) work, they discussed the possible underestimation of the absorption efficiency in the experiment due to the prepulse effect at the high laser intensity above 1×10^{14} W/cm^2.

Figure 9 presents the comparison of the simulation results to the experimental data and the HYADES predictions for 800 nm laser pulses.

The model tends to overestimate the absorption of 800 nm laser pulses at the laser intensity range above 5×10^{12} W/cm^2. A possible explanation for that is the interband absorption was not taken into account. Aluminum has an interband absorption peak at 1.55 eV which corresponds exactly to the 800 nm photon energy (Hughes *et al.*, 1969). At the laser intensities above 1×10^{14} W/cm^2, the prepulse effect may also contribute to the lower experimental values for the laser absorption, as suggested by Fisher *et al.* (2001).

Next, we compared the simulation predictions for absorption in copper for 800 nm laser pulses to the available experimental data, as shown in Figure 10.

We observed a good correlation between numerically simulated and the experimental data for copper on the laser intensity range from 5×10^{11} to 1×10^{15} W/cm^2. The interband absorption does not plays a significant role in this intensity range due to the fact that, in copper, the *d*-band lays 2.0–2.2 eV below Fermi level, and interband absorption of 800 nm photons is negligibly small, except for the very high laser intensities (Fisher *et al.*, 2005).

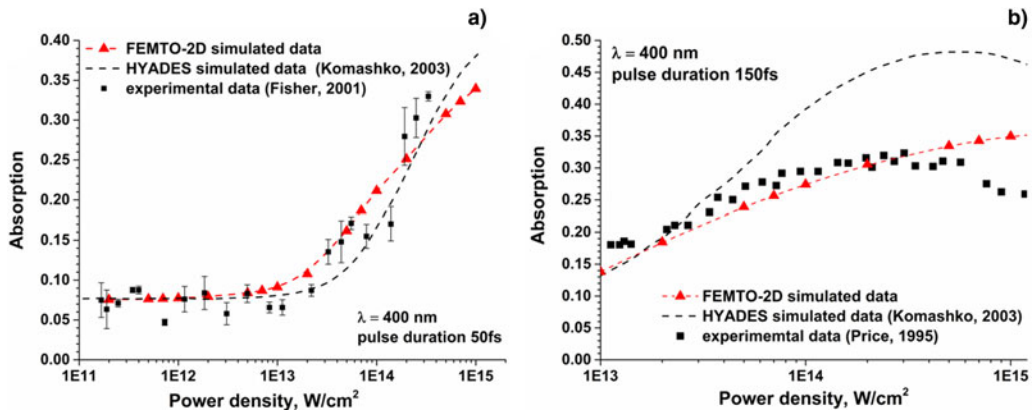

Fig. 8. Comparison of the FEMTO-2D prediction with experimental results [adopted from Fisher *et al.* (2001) and Price *et al.* (1995)] and data simulated with HYADES code [adopted from Komashko (2003)] for 400 nm wavelength. Lines guide the eye.

https://doi.org/10.1017/S0263034617000404 Published online by Cambridge University Press

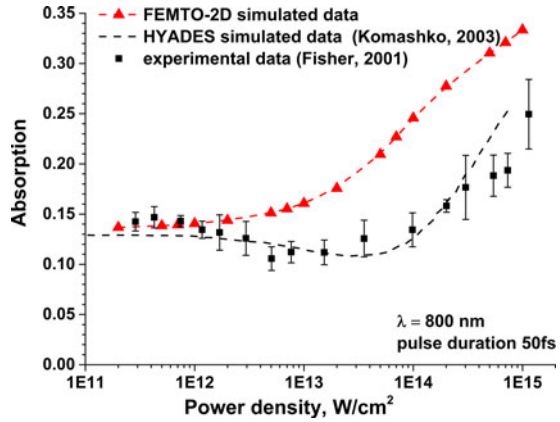

Fig. 9. Comparison of the FEMTO-2D prediction for aluminum with experimental results [adopted from Fisher *et al.* (2001)] and data simulated with HYADES code [adopted from Komashko (2003)] for 800 nm wavelength. Lines guide the eye.

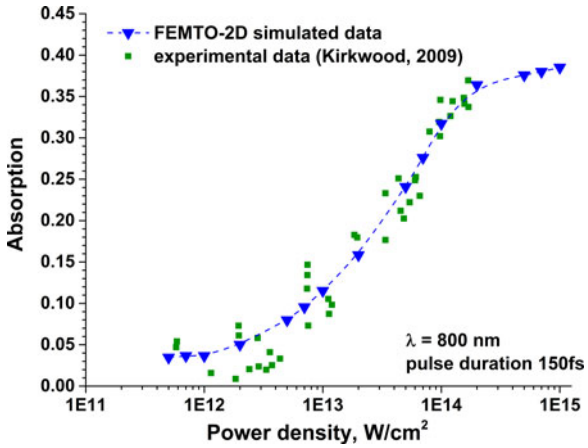

Fig. 10. Comparison of the FEMTO-2D prediction for copper with experimental results [adopted from Kirkwood *et al.* (2009)].

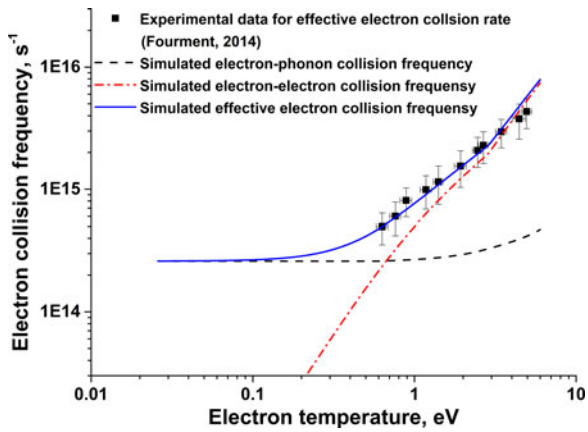

Fig. 11. Comparison of the experimental [adopted from Fourment *et al.* (2014)] and FEMTO-2D simulated data for the effective electron collision frequency in gold.

Lastly, we compared the simulation predictions for effective collision frequency in gold to the available experimental data, as shown in Figure 11.

One can see a good correlation between FEMTO-2D simulation data and the experimental results for gold at electron temperature range from about 0.5 to 6 eV. Figure 11 demonstrates the significant contribution of the electron–electron collisions to the total effective collision frequency at the electron temperature as low as 0.7 eV as it was also predicted with our model. The fact that the collision processes in the target greatly define the laser absorption efficiency allows us to assume that the simulation model should be able to correctly predict the optical properties.

4. CONCLUSION

In this manuscript, a theoretical model based on the collision theory has been presented to simulate the absorption of the ultrashort pulse laser at normal incidence by the solid metal targets in a wide laser intensity range (5×10^{11}–1×10^{15} W/cm^2). A modified two-temperature 2D model considering temperature-dependent optical and thermal physical parameters for electron and lattice subsystems was developed. For this model, we aimed to reduce the number of fitted parameters for thermodynamic parameters by utilizing theoretical formulas based on the collision theory for extreme material states namely, the cold solid state and the dense plasma state, and to decrease the calculation time by using interpolation between these states. Therefore, accurate assessment of the collision frequencies through different material states was required. Since the pulse duration for femtosecond laser is significantly shorter than thermal equilibration and material expansion time, we have assumed that the target remains at the solid density through the entire laser–target interaction process. Consequently, we modified the formula of the electron–ion collision frequency for the hot plasma state to account for electron degeneracy effect in the hot dense plasma. Moreover, although electron–electron collision frequency often assumed to be negligibly small in the hot plasma state, it had to be included in the effective collision frequency calculation for the case of the dense plasma and also for the transition stage between cold solid and dense plasma states, due to high plasma density and strong thermal non-equilibrium between electrons and lattice (Komashko, 2003; Shternin & Yakovlev, 2006).

A series of simulations were performed to predict the femtosecond laser absorption in the aluminum, gold, copper, molybdenum, and nickel targets at different laser intensities. Significant increase of the laser absorption parameter with the laser intensity was observed for aluminum, gold, and copper, and considerably smaller changes for molybdenum and nickel. We have attributed such trends to the specific details of the electron DOS distribution in these.

Finally, the model was benchmarked against experimental results for aluminum, gold, and copper – the metals that exhibit the largest changes in optical properties as function of

https://doi.org/10.1017/S0263034617000404 Published online by Cambridge University Press

temperature. The simulation predictions were found to be in a good agreement with available experimental data in a wide laser intensity range up to 10^{15} W/cm^2. However, at much higher laser intensity, considerable material expansion may occur during the laser pulse, especially for longer pulses, making the assumption of constant material density to be less accurate, and the models may need further improvements.

With this work, we have demonstrated that although utilizing constant values for reflectivity and optical depth simplifies the TTM and allows shorter calculation time for qualitative analysis of materials thermal response to the USPL irradiation, it could result in values significantly different from the case when temperature dependence of those parameters is taken into account. The evaluation of the ultrashort pulse laser absorption efficiency as a temperature-dependent parameter will allow more accurate simulation of the target thermal response in the applications where it is critical, such as prediction of the material damage threshold, laser ablation threshold, and the ablation profile.

ACKNOWLEDGMENTS

This work is partially supported by the NSF, PIRE project.

REFERENCES

Anisimov, S.I., Kapeliovich, B.L. & Perelman, T.L. (1974). Electron emission from metal surfaces exposed to ultrashort laser pulses. *J. Exp. Theor. Phys*. **66**, 776–781.

Ashcroft, N.W. & Mermin, N.D. (1976). *Solid State Physics*. New York: Holt, Rinehart and Winston.

Brown, M.S. & Arnold, C.B. (2010). Fundamentals of laser-material interaction and application to multiscale surface modification. In *Laser Precision Microfabrication* (Sugioka, K., Meunier, M. & Pique, A., Eds), pp. 91–120. Berlin, Heidelberg: Springer.

Callen, J.D. (2006). Coulomb collisions. In *Fundamentals of Plasma Physics*, available at: http://homepages.cae.wisc.edu/~callen/.

Chase, M.W. & National Institute of Standards and Technology (U.S.) (1998). *NIST-JANAF Thermochemical Tables*. 4th edn. New York: American Chemical Society.

Chen, A.M., Jiang, Y.F., Sui, L.Z., Ding, D.J., Liu, H. & Jin, M.X. (2011*a*). Thermal behavior of thin metal films irradiated by shaped femtosecond pulse sequences laser. *Opt. Commun*. **284**, 2192–2197.

Chen, A.M., Jiang, Y.F., Sui, L.Z., Liu, H., Jin, M.X. & Ding, D.J. (2011*b*). Thermal analysis of double-layer metal films during femtosecond laser heating. *J. Opt*. **13**, 55503.

Chen, A.M., Xu, H.F., Jiang, Y.F., Sui, L.Z., Ding, D.J., Liu, H. & Jin, M.X. (2010). Modeling of femtosecond laser damage threshold on the two-layer metal films. *Appl. Surf. Sci*. **257**, 1678–1683.

Chen, J.K. & Beraun, J.E. (2003). Modelling of ultrashort laser ablation of gold films in vacuum. *J. Opt. A: Pure Appl. Opt*. **5**, 168–173.

Chen, J.K., Latham, W.P. & Beraun, J.E. (2005). The role of electron–phonon coupling in ultrafast laser heating. *J. Laser Appl*. **17**, 63.

Chung, H.-K., Chen, M.H., Morgan, W.L., Ralchenko, Y. & Lee, R.W. (2005). FLYCHK: Generalized population kinetics and spectral model for rapid spectroscopic analysis for all elements. *High Energy Density Phys*. **1**, 3–12.

Du, G., Chen, F., Yang, Q., Si, J. & Hou, X. (2010). Ultrafast temperature relaxation evolution in Au film under femtosecond laser pulses irradiation. *Opt. Commun*. **283**, 1869–1872.

Fisher, D., Fraenkel, M., Henis, Z., Moshe, E. & Eliezer, S. (2001). Interband and intraband (Drude) contributions to femtosecond laser absorption in aluminum. *Phys. Rev. E* **65**, 6409.

Fisher, D., Fraenkel, M., Zinamon, Z., Henis, Z., Moshe, E., Horovitz, Y. & Eliezer, S. (2005). Intraband and interband absorption of femtosecond laser pulses in copper. *Laser Part. Beams* **23**, 391–393.

Fourment, C., Deneuville, F., Descamps, D., Dorchies, F., Petit, S., Peyrusse, O. & Recoules, V. (2014). Experimental determination of temperature-dependent electron-electron collision frequency in isochorically heated warm dense gold. *Phys. Rev. B* **89**, 161110.

Gamaly, E. (2011). *Femtosecond Laser-Matter Interaction : Theory, Experiments and Applications*. Singapore: World Scientific.

Hermann, J., Benfarah, M., Bruneau, S., Axente, E., Coustillier, G., Itina, T., Guillemoles, J.-F. & Alloncle, P. (2006). Comparative investigation of solar cell thin film processing using nanosecond and femtosecond lasers. *J. Phys. D Appl. Phys*. **39**, 453–460.

Hughes, A.J., Jones, D. & Lettington, A.H. (1969). Calculation of the optical properties of aluminium. *J. Phys. C: Solid State Phys*. **2**, 313.

Ibrahim, W.M.G., Elsayed-Ali, H.E., Shinn, M.D. & Bonner, C.E. (2003). Femtosecond damage threshold of multilayer metal films. *Proc. SPIE 4932, Seventh International Workshop on Laser Beam & Opt. Charact*., p. 55 (Boulder, Colorado).

Jiang, L. & Tsai, H.-L. (2005). Improved two-temperature model and its application in ultrashort laser heating of metal films. *J. Heat Transf*. **127**, 1167.

Kirkwood, S.E., Tsui, Y.Y., Fedosejevs, R., Brantov, A.V. & Bychenkov, V.Y. (2009). Experimental and theoretical study of absorption of femtosecond laser pulses in interaction with solid copper targets. *Phys. Rev. B* **79**, 144120.

Kittel, C. (2005). *Introduction to Solid State Physics*. New York: Wiley.

Komashko, A.M. (2003). *Laser–Material Interaction of Powerful Ultrashort Laser Pulses*. PhD Thesis. University of California, Davis.

Lee, J.B., Kang, K. & Lee, S.H. (2011). Comparison of theoretical models of electron-phonon coupling in thin gold films irradiated by femtosecond pulse lasers. *Mater. Trans*. **52**, 547–553.

Lide, D. (2003). *CRC Handbook of Chemistry and Physics*. 84th edn. London: CRC Press.

Lin, Z. (2007). Temperature dependences of the electron–phonon coupling, electron heat capacity and thermal conductivity in Ni under femtosecond laser irradiation. *Appl. Surf. Sci*. **253**, 6295–6300.

Lin, Z., Zhigilei, L.V. & Celli, V. (2008). Electron-phonon coupling and electron heat capacity of metals under conditions of strong electron-phonon nonequilibrium. *Phys. Rev. B* **77**, 75133.

Liu, K.-C. (2007). Analysis of thermal behavior in multi-layer metal thin films based on hyperbolic two-step model. *Int. J. Heat Mass Transf*. **50**, 1397–1407.

Loboda, P.A., Smirnov, N.A., Shadrin, A.A. & Karlykhanov, N.G. (2011). Simulation of absorption of femtosecond laser pulses in solid-density copper. *High Energy Density Phys*. **7**, 361.

Ordal, M.A., Bell, R.J., Alexander, R.W., Long, L.L. & Querry, M. R. (1987) Optical properties of Au, Ni, and Pb at submillimeter wavelengths. *Appl. Opt*. **26**, 744.

Ordal, M.A., Bell, R.J., Alexander, R.W., Newquist, L.A. & Querry, M.R. (1988). Optical properties of Al, Fe, Ti, Ta, W, and Mo at submillimeter wavelengths. *Appl. Opt*. **27**, 1203.

Pisonero, J., Koch, J., Wälle, M., Hartung, W., Spencer, N.D. & Günther, D. (2007). Capabilities of femtosecond laser ablation inductively coupled plasma mass spectrometry for depth profiling of thin metal coatings. *Anal. Chem*. **79**, 2325–2333.

Polek, M. (2015). *Effects of femtosecond laser irradiation of metallic and dielectric materials in the low-to-high fluence regimes*. PhD Thesis. Purdue University.

Price, D.F., More, R.M., Walling, R.S., Guethlein, G., Shepherd, R.L., Stewart, R.E. & White, W.E. (1995). Absorption of ultrashort laser pulses by solid targets heated rapidly to temperatures 1–1000 eV. *Phys. Rev. Lett*. **75**, 252–255.

Qiu, T.Q. & Tien, C.L. (1993). Heat transfer mechanisms during short-pulse laser heating of metals. *J. Heat Transf*. **115**, 835.

Qiu, T.Q. & Tien, C.L. (1994). Femtosecond laser heating of multilayer metals – I. Analysis. *Int. J. Heat Mass Transf*. **37**, 2789–2797.

Rakić, A.D., Djurišić, A.B., Elazar, J.M. & Majewski, M.L. (1998). Optical properties of metallic films for vertical-cavity optoelectronic devices. *Appl. Opt*. **37**, 5271.

Rethfeld, B., Kaiser, A., Vicanek, M. & Simon, G. (2002). Ultrafast dynamics of nonequilibrium electrons in metals under femtosecond laser irradiation. *Phys. Rev. B* **65**, 214303.

Samsonov, G.V. (1968). *Handbook of the Physicochemical Properties of the Elements*. Boston, MA: Springer US.

Shternin, P.S. & Yakovlev, D.G. (2006). Electron thermal conductivity owing to collisions between degenerate electrons. *Phys. Rev. D* **74**, 43004.

Sigman, M.E. (2010). Application of laser-induced breakdown spectroscopy to forensic science: analysis of paint and glass samples. Final Technical Report, Award No: 2004-IJ-CX-K031.

Spitzer, L. & Härm, R. (1953). Transport phenomena in a completely ionized gas. *Phys. Rev*. **89**, 977–981.

Waldecker, L., Bertoni, R., Ernstorfer, R. & Vorberger, J. (2016). Electron-phonon coupling and energy flow in a simple metal beyond the two-temperature approximation. *Phys. Rev. X* **6**, 21003.

Wang, H., Dai, W. & Melnik, R. (2006). A finite difference method for studying thermal deformation in a double-layered thin film exposed to ultrashort pulsed lasers. *Int. J. Therm. Sci*. **45**, 1179–1196.

Wang, S.Y., Ren, Y., Cheng, C.W., Chen, J.K. & Tzou, D.Y. (2013). Micromachining of copper by femtosecond laser pulses. *Appl. Surf. Sci*. **265**, 302–308.

Watling, R.J., Lynch, B.F. & Herring, D. (1997). Use of laser ablation inductively coupled plasma mass spectrometry for fingerprinting scene of crime evidence. *J. Anal. At. Spectrosc*. **12**, 195–203.

Wellershoff, S.-S., Hohlfeld, J., Güdde, J. & Matthias, E. (1999). The role of electron–phonon coupling in femtosecond laser damage of metals. *Appl. Phys. A* **69**, 99–107.

Zhang, B., He, M., Hang, W. & Huang, B. (2013). Minimizing matrix effect by femtosecond laser ablation and ionization in elemental determination. *Anal. Chem*. **85**, 4507–4511.

Zhang, J., Chen, Y., Hu, M. & Chen, X. (2015). An improved three-dimensional two-temperature model for multi-pulse femtosecond laser ablation of aluminum. *J. Appl. Phys*. **117**, 63104.

Zhao, X. (2014). *Ultrashort laser pulse–matter interaction: Fundamentals and early stage plasma dynamics*. PhD Thesis. Purdue University.